Computational Study of Particle Deposition in Patient Specific Geometries

Marika Pilou, Anastasios Skiadopoulos, Evangelos Makris, Panagiotis Neofytou, and Christos Housiadas

***Abstract*—The present work focuses on the study of particle deposition in segments of the cardiovascular system. In particular, the geometry of an iliac bifurcation is reconstructed from medical imaging data and the flow fields of both blood and particles are obtained using Computational Fluid Particle Dynamics techniques. Particle convection, diffusion and inertia are taken into account in the simulations. The numerical experiments indicate that diffusion dominates deposition and only 10% of the injected particles deposit in the bifurcation. Both blood flow field and the characteristics of the patient specific geometry influence the particle deposition sites. Overall, the proposed methodology could become a useful tool for the design and optimization of biomedical applications.**

I. Introduction

New possibilities in medicine arise through the development of micro/nano drugs and diagnostic systems. Among the various proposed biomedical uses of particles, there are applications related to cancer diagnosis and therapy, stem cell therapy, advanced drug delivery systems and medical imaging [1-4]. The behavior of particles in the circulatory system for therapeutic and/or diagnostic purposes is today a topic of high scientific interest [5, 6].

In the present study, we employ Computational Fluid Particle Dynamics (CFPD) techniques in order to study the flow of particles in segments of the human cardiovascular system. The effects of particle convection, diffusion and inertia are taken into account. As a test case, particle deposition is calculated in an iliac bifurcation (IB), the geometry of which is reconstructed from medical imaging data, assuming pulsating blood flow.

II. Methods

A. Grid Generation

The computational grid is generated on an IB via an in-house code which processes medical imaging data and generates multi-block structured computational grids [7].

The patient specific geometry data are acquired by medical imaging techniques in Digital Imaging and Communications in Medicine (DICOM) format. The grid generation procedure consists of the following consecutive steps; (a) the volume of interest is extracted and a three dimensional triangulated surface representing the bifurcation geometry is created by means of the medical imaging software, (b) the triangulated surface is split and on each subdomain a multi block surface structured grid is generated, and (c) the branches of the surface grid are unified and the volume grid inside the domain is generated.

In the present study, anonymous patient data by Computed Tomography were used. In Fig. 1, the reconstructed IB geometry and the structured computational grid are illustrated. The grid consists of 319,616 computational nodes.

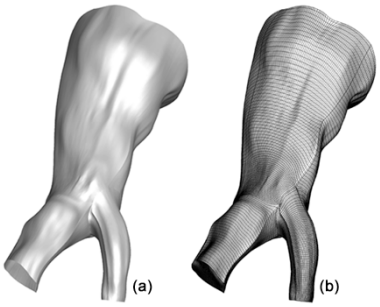

Fig.1. View of (a) the reconstructed iliac bifurcation surface geometry and (b) the structured computational grid.

B. Continuous Phase

The governing equations for the three dimensional (3D) flow field of an incompressible Newtonian fluid are the mass continuity and momentum (Navier-Stokes) equations. In particular, if $\vec{v} = u\hat{i} + v\hat{j} + w\hat{k}$ is the fluid velocity, $d\vec{S} = \hat{n}\,dS$ the elemental surface vector with $\hat{n}$ the normal to the surface unit vector, $d\Omega$ the elemental volume, t the time and $\hat{i}, \hat{j}, \hat{k}$ the Cartesian basis vectors, then in dimensionless and integral form the mass continuity equation is written as:

$$\int_S \vec{v} \cdot d\vec{S} = 0 \,, \quad (1)$$

whereas the Navier-Stokes equations in 3D Cartesian coordinates x, y and z are written, respectively, as:

$$\frac{d}{dt}\int_\Omega u\,d\Omega + \int_S u\vec{v}\cdot d\vec{S} = -\int_S p\hat{i}\cdot d\vec{S} + \frac{1}{\mathrm{Re}}\int_S (\tau_{xx}\hat{i} + \tau_{yx}\hat{j} + \tau_{zx}\hat{k})\cdot d\vec{S} \,, \quad (2a)$$

$$\frac{d}{dt}\int_\Omega v\,d\Omega + \int_S v\vec{v}\cdot d\vec{S} = -\int_S p\,\hat{j}\cdot d\vec{S} + \frac{1}{\mathrm{Re}}\int_S (\tau_{xy}\hat{i} + \tau_{yy}\hat{j} + \tau_{zy}\hat{k})\cdot d\vec{S} \,, \quad (2b)$$

Manuscript received September 19, 2013.

M. Pilou (corresponding author, phone: +30 210 6503700; fax: +30 210 6545496; e-mail: pilou@ipta.demokritos.gr), A. Skiadopoulos, E. Makris, P. Neofytou and C. Housiadas are with the Thermal Hydraulics & Multiphase Flow Laboratory, INRASTES, NCSR "Demokritos", Agia Paraskevi, 15310, Greece. (e-mail: tskiado@ipta.demokritos.gr, vagmakr@ipta.demokritos.gr, panosn@ipta.demokritos.gr, christos@ipta.demokritos.gr)

978-1-4799-3163-7/13/$31.00 ©2013 IEEE

$$\frac{d}{dt}\int_{\Omega} w d\Omega + \int_{s} w\vec{v}\cdot d\vec{S} = -\int_{s} p\hat{k}\cdot d\vec{S} + \frac{1}{\mathrm{Re}}\int_{s}(\tau_{xz}\hat{i} + \tau_{yz}\hat{j} + \tau_{zz}\hat{k})\cdot d\vec{S} \quad (2c)$$

where τ_{ij} are the Cartesian components of the stress tensor and p is the fluid pressure. Equations (1) and (2) are normalized using the parent vessel diameter, $d_1 (= 2r_1)$, to scale lengths and the maximum inlet fluid velocity, $\upsilon_{\max}$, to scale the velocities. Moreover, time is scaled with $t_0 = d_1/\upsilon_{\max}$, whereas $\rho_f \upsilon_{\max}^2$ and $\upsilon_{\max}/d_1$ are used for making dimensionless the pressure and the shear stress terms, respectively. In (2), Re is the fluid flow Reynolds number, defined as $\mathrm{Re} = (d_1 \upsilon_{\max} \rho_f)/\mu_f$, with ρ_f the fluid density and μ_f the fluid dynamic viscosity.

The dimensionless mass continuity and Navier-Stokes equations are solved numerically using an in-house CFD code [8, 9]. The code employs the SIMPLE algorithm of [10] in conjunction with a finite-volume method (FVM) on multi-block, collocated, body-fitted 3D grids, where grid non-orthogonality is taken into account. Equations (2) are discretized using a first-order forward Euler scheme for the time dependent term, a third-order QUICK scheme for the convective term and a central difference scheme (CDS) of second-order for the diffusion (viscous) term, whereas the pressure term is treated as source [11]. The code is parallelized via a domain decomposition technique, applying a Single Program Multiple Data (SPMD) style of parallel implementation. Communication between processes is accomplished through the Message Passing Interface (MPI) message passing system, due to its high communication performance and portability. Flow field simulations where performed on a High Performance Computing (HPC) Rocks Cluster. Herein, the IB domain was decomposed into two subdomains, and the computational load was equally distributed to the computational nodes in order to minimize the processors idle time and the total execution overhead.

C. *Particulate Phase*

If c is the particle mass concentration and $\vec{v}_p$ the particle velocity, then the mass conservation equation of the particulate phase is written as:

$$\partial c/\partial t + \nabla\cdot(c\vec{v}_p) = 0\,, \quad (3)$$

To incorporate particle inertial effects on Brownian diffusive transport, [12] used a first order correction of particle velocity in particle relaxation time based on the work of [13]. Particle velocity can be approximated by:

$$\vec{v}_p = \vec{\upsilon} - \tau_p\left(\partial\vec{\upsilon}/\partial t + \vec{\upsilon}\cdot\nabla\vec{\upsilon}\right) - D\nabla\ln c + O\left(\tau_p^2\right), \quad (4)$$

where $\tau_p = \rho_p d_p^2/18\mu_f$ the particle relaxation time and $D = k_B T_f/3\pi\mu_f d_p$ the Stokes-Einstein diffusion coefficient. In these relationships, k_B is the Boltzmann's constant, T_f is the fluid temperature and ρ_p and d_p are the particle density and diameter, respectively.

Particle velocity is, thus, decomposed into a diffusive part, dependent only on the particle concentration gradient, and a convective part, $\vec{v}_c$, that equals:

$$\vec{v}_c = \vec{\upsilon} - \tau_p\left(\partial\vec{\upsilon}/\partial t + \vec{\upsilon}\cdot\nabla\vec{\upsilon}\right) \quad (5)$$

The convective velocity incorporates the inertial effects of the particulate phase and depends only on the fluid field and the particle relaxation time.

Introducing the approximation of the particle velocity into (3), we obtain:

$$\partial c/\partial t + \nabla\cdot(c\vec{v}_c) = \nabla\cdot(D\nabla c)\,. \quad (6)$$

Equation (6) is a modified steady-state convective diffusion equation, which in dimensionless and integral form is written as (to simplify notation we retain the same variables to denote dimensionless quantities):

$$\int_{\Omega}\partial c/\partial t\, d\Omega + \int_{S} c\vec{v}_c\cdot\vec{dS} = Pe^{-1}\int_{S}\nabla c\cdot\vec{dS}\,, \quad (7)$$

where the dimensionless convective velocity is equal to:

$$\vec{v}_c = \vec{\upsilon} - St\left(\partial\vec{\upsilon}/\partial t + \vec{\upsilon}\cdot\nabla\vec{\upsilon}\right), \quad (8)$$

In the previous equations, $St = \tau_p \upsilon_{\max}/d_1$ is the particle Stokes number and $Pe = d_1\upsilon_{\max}/D$ is the mass Peclet number, a function of the particle diameter through D. Equations (7)-(8), describe particle convection, inertia and diffusion in an Eulerian formulation.

The modified convection-diffusion equation, (7), is solved assuming (dimensionless) parabolic concentration profile at the inlet of the IB. Moreover, the totally absorbing wall boundary condition is imposed on the walls of the bifurcation:

$$c\big|_w = 0\,, \quad (9)$$

The total (dimensionless) deposition flux towards the wall will be equal to:

$$F_{dep} = F^c\big|_w + F^d\big|_w\,, \quad (10)$$

where $F^d\big|_w$ the diffusive flux:

$$F^d\big|_w = -Pe^{-1}\int_{S}\nabla c\cdot\vec{dS}\Big|_w\,, \quad (11)$$

and $F^c\big|_w$ the convective flux:

$$F^c\big|_w = \begin{cases} 0 & \text{if } \vec{v}_c\cdot\vec{dS}\big|_w \le 0 \\ \int_{S} c\vec{v}_c\cdot\vec{dS}\big|_w & \text{if } \vec{v}_c\cdot\vec{dS}\big|_w > 0 \end{cases}. \quad (12)$$

The particle convective velocity in (12) is calculated at the computational grid point closest to the wall.

Equation (7) with the appropriate boundary conditions is solved numerically using an in-house CFPD-based code [12]. The code calculates the convective velocity of the particles by the fluid velocity, through (8), and then proceeds to the solution of the modified convection-diffusion equation in three dimensions using a FVM. In the code, a first-order forward Euler discretisation scheme is employed for the time dependent term, whereas the convective term is discretized using a second-order deferred correction and a second-order

central difference scheme is preferred for the diffusive term [11].

III. Results & Discussion

A. Continuous Phase

In the present study, blood is assumed a Newtonian fluid with dynamic viscosity $\mu_f = 0.004 kg/m \cdot s$ and density $\rho_f = 1055 kg/m^3$. The radius of the parent vessel of the IB is $r_1 = 6 \cdot 10^{-3} m$. Blood flow is considered laminar, incompressible and pulsating with time period of 1s, which is typical of blood flow simulations. The flow field of Fig. 2 is imposed at the inlet assuming at each time step a fully developed parabolic profile. The time varying flow profile at the inlet complies with physiological conditions, since blood flow measurements indicate that the velocity profiles changes from being almost flat in the aorta to an almost parabolic shape in smaller arteries [14]. In the present case, the maximum flow over a period of 1s is $Q_{\max} = 9.6698 \cdot 10^{-6} m^3/s$, which corresponds to maximum velocity $u_{\max} = 0.0855 m/s$, thus $\mathrm{Re} = 270$.

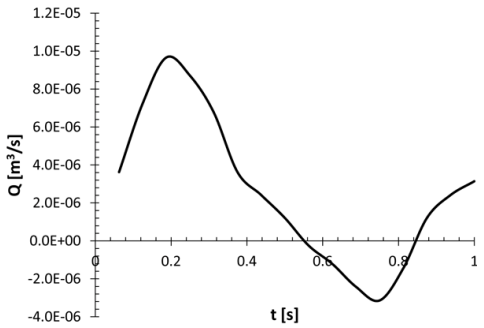

Fig.2. Fluid flow, Q, at the inlet of the iliac bifurcation over 1s.

At the bifurcation branches outlets, which are considered to be open boundaries, the following boundary condition is implemented:

$$p = p_s + \nu \left(d\upsilon_n / d\hat{n} \right). \quad (13)$$

In (13), p_s is a specified value of pressure, $\nu = 1/\mathrm{Re}$ is the diffusion coefficient and $\upsilon_n = \vec{\upsilon} \cdot \hat{n}$. Herein, p_s was chosen to be equal to 0 for both branches of the bifurcation. The specified outlet pressure boundary condition is the most common in blood flow simulations and ensures that the numerical scheme is well posed and the obtained solution is unique [15].

In Fig. 3, velocity magnitude contours on a plane parallel to the centreline of the domain, as well as velocity vectors at sections crossing the inlet of the parent vessel, outlet of the branches and immediately downstream of the bifurcation are presented at three characteristics timesteps. These timesteps correspond to the maximum positive fluid flow (t=0.1875s), the first instance that the flow becomes negative (t=0.5625s) and the maximum negative fluid flow (t=0.75s).

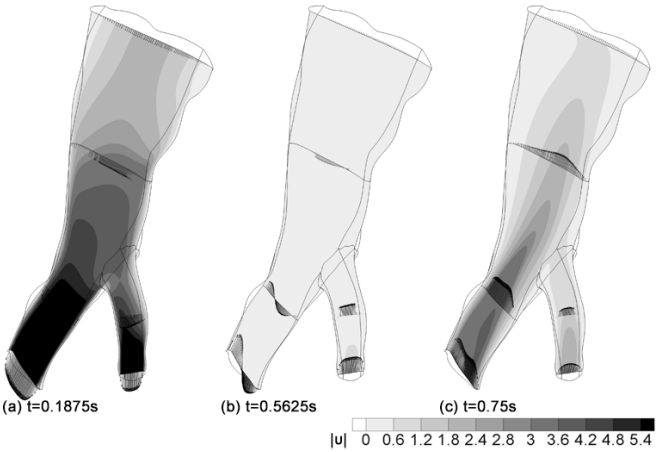

Fig.3. Velocity magnitude contours on a plane parallel to the centreline of the IB and velocity vectors at characteristic cross sections.

B. Particulate Phase

For the particulate phase simulations, we assume spherical particles consisting of 67.5% iron and 32.5% carbon (by weight), which have density ρ_p=6450 kg/m^3 and have applications as drug carriers in the cardiovascular system [16]. The particle diameter is taken equal to d_p=1μm. Particle release at the inlet over 1s (i.e. one fluid flow field period) is assumed and then the particle flow is calculated for further 9s. The inlet, outlet and wall concentration fluxes over time are shown in Fig. 4. The numerical experiment showed that with the given fluid flow conditions only 1.5s are needed after the end of release in order for the particles to either exit or deposit on the walls of the iliac bifurcation.

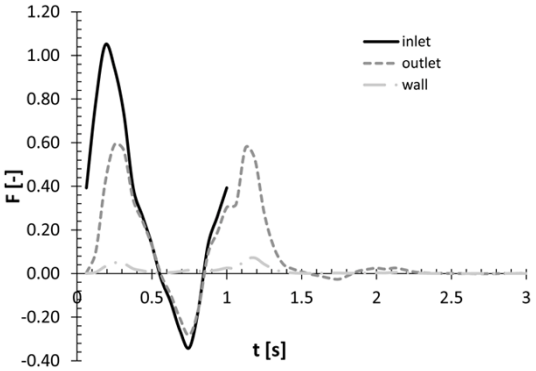

Fig.4. Dimensionless concentration flux, F, over time.

Moreover, the particles deposition fraction, defined as:

$$\eta = \frac{m_{dep}^{tot}}{m_{in}^{tot}} \times 100\%, \quad (14)$$

where m_{dep}^{tot} and m_{in}^{tot} are, respectively, the total mass of particles deposited on the walls and those that entered the bifurcation during the time period of reference (i.e. 10s), is found equal to 9.93%. In fact, the combination of particle convection due to the pulsating field with the complex IB geometry results in transfer of particles from the bulk flow to the vicinity of the bifurcation walls. Sensitivity studies showed that from there particles deposit mainly due to diffusion, rather than inertia. This fact is attributed to the

high blood dynamic viscosity that gives rise to very low particle relaxation times, i.e. the particles follow closely the fluid flow. Deposition due to diffusion is also the reason for the low deposition fraction; diffusion is a relative slow process comparing to the bulk particle transport due to convection.

In Fig. 5, the particles deposition sites are shown for the characteristic timesteps during the first (top row) and second (bottom row) fluid flow field periods. It can be seen that for Q>0 (Fig. 5(a) and (d)), there is strong deposition at the top of the carinal ridge, whereas for Q<0 particles deposit mainly at the bifurcation branches. The deposition patterns for the corresponding timesteps in the two periods are equivalent, although actual deposition is less during the second period as there is no release of new particles. In all cases, however, we notice that deposition also occurs in areas of the bifurcation, where the geometry has folds and twists. It should be noted that in Fig. 5, the local deposition enhancement factor (EF) rather than the deposition particle flux is depicted. This factor is defined as the ratio of the deposition density in a given subarea of the bifurcation to the deposition density in the whole bifurcation and takes into account the fact that the wall faces of the grid are not of the same size.

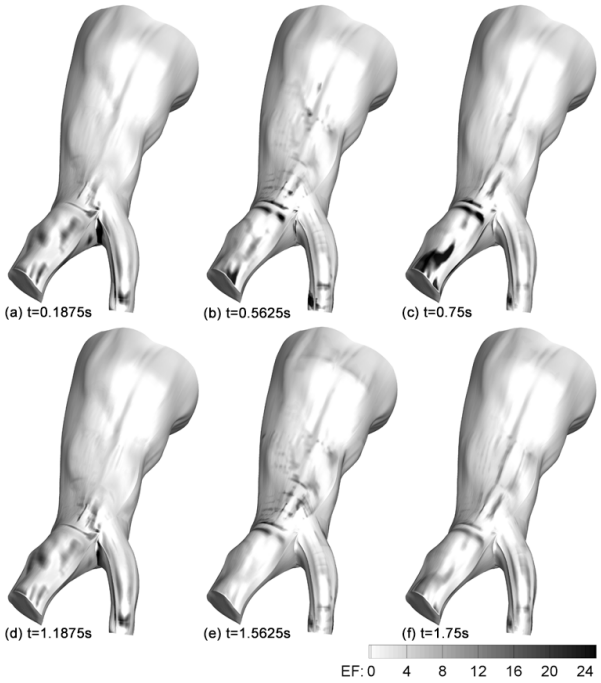

Fig.5. Local deposition enhancement factor (EF) at the bifurcation walls.

IV. Conclusion

Particle deposition in a patient specific iliac bifurcation assuming pulsating blood flow was studied using CFPD techniques, taking into account particle convection, diffusion and inertia. It was found that particles deposition sites depend on the fluid flow field, as well as on the characteristics of the examined geometry. In the examined case, diffusion was the main particle deposition mechanism; due to the high blood viscosity particles inertial effects are diminished. It was calculated that deposition fraction for the examined case is only 9.93%, which can be explained by the slow nature of diffusive transport. Thus, in order to achieve a specific dose of particles in this area, one should either administer higher particles doses or enhance deposition efficiency. The latter could be achieved, for example, through particle surface coating or by implementation of external force fields (magnetic or thermal).

Overall, the proposed methodology can contribute to the interpretation of observed behavior of particles in the cardiovascular system by offering better physical insight and serving as a tool for the design and optimization of biomedical applications.

References

[1] S. R. Grobmyer, D. L. Morse, B. Fletcher, L. G. Gutwein, P. Sharma, V. Krishna, et al., "The promise of nanotechnology for solving clinical problems in breast cancer," *J. Surg. Oncol. ,* vol. 103, pp. 317-325, Mar. 2011.

[2] C. Iancu, I. R. Ilie, C. E. Georgescu, R. Ilie, A. R. Biris, T. Mocan, et al., "Applications of nanomaterials in cell stem therapies and the onset of nanomedicine," *Particulate Sci. Technol.,* vol. 27, pp. 562-574, Nov. 2009.

[3] A. Kumar, P. K. Jena, S. Behera, R. F. Lockey, S. Mohapatra, and S. Mohapatra, "Multifunctional magnetic nanoparticles for targeted delivery," *Nanomedicine: NBM,* vol. 6, pp. e64-e69, Feb. 2010.

[4] M. Slevin, L. Badimon, M. Grau-Olivares, M. Ramis, J. Sendra, M. Morrison, et al., "Combining nanotechnology with current biomedical knowledge for the vascular imaging and treatment of atherosclerosis," *Mol. Biosyst.,* vol. 6, pp. 444-450, 2010.

[5] A. S. Gupta, "Nanomedicine approaches in vascular disease: a review," *Nanomedicine: NBM,* vol. 7, pp. 763-779, Dec. 2011.

[6] V. Karagkiozaki, "Nanomedicine highlights in atherosclerosis," *J. Nanopart. Res.,* vol. 15, p. 1529, Mar. 2013.

[7] E. Makris, P. Neofytou, S. Tsangaris, and C. Housiadas, "A novel method for the generation of multi-block computational structured grids from medical imaging of arterial bifurcations," *Med. Eng. Physics,* vol. 34, pp. 1157-1166, Oct. 2012.

[8] P. Neofytou and S. Tsangaris, "Flow effects of blood constitutive equations in 3D models of vascular anomalies," *Int. J. Num. Methods Fluids,* vol. 51, pp. 489-510, June 2006.

[9] P. Neofytou, S. Tsangaris, and M. Kyriakidis, "Vascular wall flow-induced forces in a progressively enlarged aneurysm model," *Comput. Method. Biomech. Biomed. Eng.,* vol. 11, pp. 615-626, June 2008.

[10] S. V. Patankar, *Numerical Heat Transfer and Fluid Flow*: Taylor & Francis, 1980.

[11] J. H. Ferziger and M. Perić *Computational Methods for Fluid Dynamics*: Springer, 2002.

[12] M. Pilou, S. Tsangaris, P. Neofytou, C. Housiadas, and Y. Drossinos, "Inertial particle deposition in a 90-degree laminal-flow bend: An Eulerian fluid-particle approach," *Aerosol Sci. Technol.,* vol. 45, pp. 1376-1387, Nov. 2011.

[13] J. Fernandez de la Mora and D. E. Rosner, "Effects of inertia on the diffusional deposition of small particles to spheres and cylinders at low Reynolds numbers," *J. Fluid Mech.,* vol. 125, pp. 379-395, Dec. 1982.

[14] D. A. McDonald, *Blood flow in arteries*, 2nd ed. London: Edward Arnold, 1974.

[15] J. G. Heywood, R. Rannacher, and S. Turek, "Artificial boundaries and flux and pressure conditions for the incompressible Navier-Stokes equations," *Int. J. Num. Methods Fluids,* vol. 22, pp. 325-352, Aug. 1996.

[16] J. W. Haverkort, S. Kenjereš, and C. R. Kleijn, "Computational simulations of magnetic particle capture in arterial flows," *Ann. Biomed. Eng.,* vol. 37, pp. 2436-2448, Dec. 2009.